J. Fluid Mech. (2008), *vol.* 614, *pp.* 471–493. © 2008 Cambridge University Press
doi:10.1017/S0022112008003649 Printed in the United Kingdom

Wetting failure and contact line dynamics in a Couette flow

M. SBRAGAGLIA[1], K. SUGIYAMA[2] AND L. BIFERALE[1]

[1]Department of Physics and INFN, University of Tor Vergata, Via della Ricerca Scientifica 1, 00133 Rome, Italy

[2]Department of Mechanical Engineering, The University of Tokyo, 7-3-1 Hongo Bunkyo-Ku, Tokyo 113-8656, Japan

(Received 16 May 2008 and revised form 3 August 2008)

Liquid–liquid wetting failure is investigated in a two-dimensional Couette system with two immiscible fluids of arbitrary viscosity. The problem is solved exactly using a sharp interface treatment of hydrodynamics (lubrication theory) as a function of the control parameters – capillary number, viscosity ratio and separation of scale – i.e. the slip length versus the macroscopic size of the system. The transition at a critical capillary number, from a stationary to a non-stationary interface, is studied while changing the control parameters. Comparisons with similar existing analyses for other geometries, such as the Landau–Levich problem, are also carried out. A numerical method of analysis is also presented, based on diffuse interface models obtained from multiphase extensions of the lattice Boltzmann equation. Sharp interface and diffuse interface models are quantitatively compared, indicating the correct limit of applicability of the diffuse interface models.

1. Introduction

Despite many years of research, the physics of moving contact lines (De Gennes 1985; Oron, Davis & Bankoff 1997; Blake 2006) is still not completely understood. This lack of understanding stems from different factors. Dynamical wetting operates on scales extending from the macroscopic to the molecular. At those scales, given the small Reynolds numbers achieved in such motion, viscous forces are balanced with surface tension effects (Voinov 1976; De Gennes 1985; Cox 1986). A dimensionless measure of this balance is provided by the capillary number $Ca = \mu U/\sigma$, comparing the viscous term at the contact line ηU with the surface tension σ, where η denotes the liquid viscosity and U the contact line velocity. Liquid motion at finite capillary numbers induces changes in the shape of the interface, and the resulting macroscopic dynamic angle $\theta_M(Ca)$ is different from its static equilibrium counterpart. Within this context, the main issue in contact line research is to relate the macroscopic angle to the inner physics, with particular emphasis on the mechanisms removing the small-scale singularities (Voinov 1976; Cox 1986; De Gennes 1986). In fact, it is well known that the viscous stress diverges at the contact line if some physical mechanism is not introduced to remove the singularity (Dussan 1979; De Gennes 1986; Pismen & Pomeau 2000). To overcome this problem, numerous proposals have been made (Huh & Scriven 1971; Voinov 1976; Hocking & Rivers 1982; De Gennes 1985; Cox 1986; Dussan, Rame & Garoff 1991), all of them leading to the introduction of a small-length-scale parameter ℓ_s used to remove the viscous singularity. An example

https://doi.org/10.1017/S0022112008003649 Published online by Cambridge University Press

is provided by the slip length at the boundaries, where this small-scale parameter is related to the presence of a finite slip (Huh & Scriven 1971; Cox 1986). Also, other mechanisms such as intermolecular forces (De Gennes 1986; Jacqmin 2000; Pismen & Pomeau 2000; Ding & Spelt 2007) in the immediate vicinity of the contact line can be considered.

Once the small-scale singularity is removed, the macroscopic angle emerges as a function of the capillary number $\theta_M(Ca)$. Although the explicit forms may clearly depend on the specific model used to remove the singularity, the common feature is that the small capillary-number limit scales linearly with the contact line velocity, i.e. $\theta_M(Ca) \sim Ca$ (Voinov 1976; Cox 1986). Differences are expected to emerge close to the wetting transition. When the liquid advances, a critical speed exists above which a stationary contact line cannot be sustained any longer, and liquid deposition may occur on the solid (Blake & Ruschak 1979; De Gennes 1986; Quéré 1991; Sedev & Petrov 1991; Podgorski, Flesselles & Limat 2001; Simpkins & Kuck 2003; Eggers 2004*a*; Jacqmin 2004; Snoeijer *et al.* 2007). The understanding of this transition is crucial. In fact, the breaking of stationarity can be interpreted as a lost of universality: the hydrodynamical regime does not support any longer a time-independent solution, indicating some singular behaviour in the matching between inner and outer regions.

In his review, Kistler (1993) supports the assumption that wetting failure occurs when the dynamic angles reach zero degrees (throughout the paper notations are consistent with a macroscopic angle that decreases as the capillary number increases; see also the geometry in figure 1 with θ_M smaller than θ_m), whereas the contact line is observed to become V-shaped in the vicinity of the instability (Blake & Ruschak 1979; Ghannum & Esmail 1993).

Evidence for the existence of such critical points of entrainment has also been provided by some recent theoretical works. The problem has been tackled using a full hydrodynamic calculation incorporating viscous effects on all scales (Hocking 2001; Eggers 2004*a*, 2005). In particular, within the framework of the 'Landau–Levich' problem (Landau & Levich 1942; Derjaguin 1943), i.e. a plate plunging into or being withdrawn from a liquid bath, it has been shown (Eggers 2004*a*, 2005) that stationary solutions cease to exist above a critical capillary number Ca_{cr}. The value of the emerging critical capillary number is quantified exactly; although we find universal features in terms of the microscopic angle (θ_m) of the liquid at the wall ($Ca_{cr} \sim \theta_m^3$), a non-universality is also present in the geometrical prefactor depending on the angle of inclination of the plate with respect to the liquid (Eggers 2004*a*, 2005).

The whole picture is also enriched by recent experimental observations (Snoeijer *et al.* 2006), which show that the formation of solitary capillary waves can drastically change the value of the critical speeds of entrainment (pre-critical wetting transition). Along these lines, linear stability analysis (Golestanian & Raphael 2001*a*, *b*; Snoeijer *et al.* 2007) for the relaxation of external perturbations has also revealed that dispersion relations behave differently away from and close to the critical point.

Wetting failure has also been investigated in a recent paper by Jacqmin (2004), where a liquid–liquid isoviscous system in a Couette geometry was treated using various methods. This system, consisting of two walls moving with opposite velocities, has been treated in the parallel flow approximation, with the Fourier series method and also with phase field models (Jacqmin 2000, 2004). In these liquid–liquid systems, wetting failure has been found to set in well before the dynamic angle reaches zero degrees.

In this paper, we further elaborate on and explore these issues by following a double-sided strategy. First, we extend the analysis of Jacqmin (2004) to arbitrary viscosity

https://doi.org/10.1017/S0022112008003649 Published online by Cambridge University Press

ratio $\chi = \mu_g/\mu_l$, where μ_g and μ_l are the gas and liquid viscosities, respectively. We then quantify the breaking of a stationary regime at a critical capillary number $Ca_{cr}(\chi, \lambda, \theta_m)$, which depends on the viscosity ratio χ, the microscopic wettability θ_m and the ratio between inner and outer scales, $\lambda = \ell_s/H$. Here ℓ_s is the slip length associated with a finite contact line slip, and H is the distance between the two plates in the Couette geometry (see § 2). The theoretical approach used is based on the lubrication approximation, i.e. a sharp interface treatment of hydrodynamics dealing with weakly bended interfaces (Oron *et al.* 1997). In order to investigate macroscale geometry effects we also compare our results to those of a similar analysis applied to the Landau–Levich problem (Eggers 2004*a*, 2005).

In the second part of the paper we follow a computational pathway. We study the same Couette flow with multiphase extensions of the lattice Boltzmann equation (LBE) (Wolf-Gladrow 2000; Succi 2001). In these diffuse interface methods effective slip is induced by the finite width of the interface (Seppecher 1996; Ding & Spelt 2007), which is explicitly considered in the separation of two bulk phases. On one side, the LBE provides a benchmark of theory in those cases in which the analytical approach is questionable (strongly bended interfaces and/or finite contact angles). On the other side, we use the sharp interface calculation to study the effects of finite width of the interface on the system. Comparison between a sharp interface theory (with slip-removed singularity) and LBE (with diffuse-removed singularity) is a way to probe the universality of the dynamics far from the contact line; i.e. whether the latter is independent of the microscopic details used to remove the singularity.

Dynamical benchmarks of the LBE for multiphase flows are also important because of the difficulties in controlling corrections to the hydrodynamical limit in the presence of strong density gradients (Cristea & Sofonea 2003; Wagner 2003; Lee & Fischer 2006; Shan 2006; Yuan & Schaefer 2006; Sbragaglia *et al.* 2007). We show that the LBE recovers the correct hydrodynamical behaviour at large scales. The parameter-controlling deviations from sharp interface hydrodynamics will therefore be proportional to the ratio between the inner length scale (interface width) and the outer scale of the system.

2. Lubrication approach in the Couette flow

The geometry we study consists of two parallel walls moving with opposite velocities $\pm U_w$. The two walls have opposite wettability so that when the fluid is motionless the interface is a straight line angling from wall to wall (see figure 1). For each fixed horizontal (the origin of the coordinates is chosen so that the horizontal spreading of the interface is centred at $x = 0$) location (x), the interface profile is denoted by $h(x)$. Computations are carried out under the assumption of a finite and fixed slip length (ℓ_s), for simplicity the same on both walls. Other parameters are the capillary number, $Ca = U_w\mu_l/\sigma$, and the viscosity ratio, $\chi = \mu_r/\mu_l$. It is further assumed that the left fluid is the more viscous one, so that $\mu_l > \mu_r$, and consequently $\chi \leqslant 1$. The computation at $\chi = 1$ serves as the benchmark test of our results when compared to the results given in Jacqmin (2004).

Using a lubrication approximation (Oron *et al.* 1997; Jacqmin 2004; Eggers 2004*a*, 2005; Snoeijer 2005) we carry out a long wavelength expansion in the stationary equations of motion (i.e. Stokes equation and continuity equation). Therefore, the theory developed is expected to be valid in the limit of small tilting angles between the interface and the wall. In this way, for a fixed horizontal coordinate x, the

https://doi.org/10.1017/S0022112008003649 Published online by Cambridge University Press

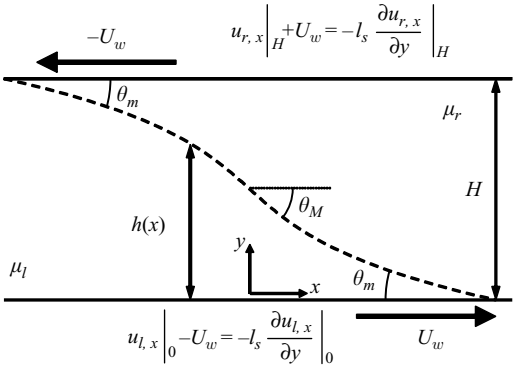


FIGURE 1. The geometry used to analyse the stability problem. Two parallel walls are moved with opposite velocities $\pm U_w$. The two fluids under consideration are distinguished as left (l, more viscous) and right (r, less viscous), and the viscosity ratio is denoted by $\chi = \mu_r/\mu_l$. The angles that the fluids form with the walls are complementary (opposite wetting properties). The microscopic angle θ_m is defined as the angle that the left fluid forms with the lower wall, and the angle θ_M is taken as the angle in the centre of the channel, with the convention that for finite capillary number θ_M is smaller that θ_m. The interface is determined by a function $h(x)$ of the horizontal coordinate. Streamwise and vertical velocity fields for the left and right fluids will respectively be denoted with $u_{l,x}$ and $u_{l,y}$ and with $u_{r,x}$ and $u_{r,y}$.

complete set of equations to be analysed is

$$\mu_l \frac{\partial^2 u_{l,x}}{\partial y^2} = \frac{\partial p_l}{\partial x}, \qquad \mu_r \frac{\partial^2 u_{r,x}}{\partial y^2} = \frac{\partial p_r}{\partial x}, \tag{2.1}$$

$$\partial_x u_{l,x} + \partial_y u_{l,y} = 0, \qquad \partial_x u_{r,x} + \partial_y u_{r,y} = 0, \tag{2.2}$$

where we respectively label with l and r the left and right fluids with viscosities μ_l and μ_r and pressures p_l and p_r. These equations are the natural generalization of those analysed in Jacqmin (2004), where the author considered the case $\mu_l = \mu_r$. The solutions for the horizontal velocities in the left and right fluids ($u_{l,x}, u_{r,x}$) are rapidly evaluated as

$$u_{l,x} = \frac{1}{\mu_l}\left(A_l + B_l y + \frac{1}{2} p_{l,x} y^2\right), \qquad u_{r,x} = \frac{1}{\mu_r}\left(A_r + B_r y + \frac{1}{2} p_{r,x} y^2\right), \tag{2.3}$$

where we have used $p_{l,x} = \partial p_l/\partial x$ and $p_{r,x} = \partial p_r/\partial x$. The vertical components $u_{l,y}$ and $u_{r,y}$ have to be evaluated from (2.2) with the usual boundary condition of zero normal velocity at the wall. Obviously, A_l, B_l, $p_{l,x}$, A_r, B_r, $p_{r,x}$ have to be determined upon the imposition of *ad hoc* boundary/matching conditions that will determine the position of the interface $h(x)$. The relevant matching conditions are the continuity of the parallel velocity and viscous stress at the interface

$$u_{l,x}|_h = u_{r,x}|_h, \qquad \mu_l \frac{\partial u_{l,x}}{\partial y}\bigg|_h = \mu_r \frac{\partial u_{r,x}}{\partial y}\bigg|_h \tag{2.4}$$

plus the lower and upper wall boundary conditions written as

$$u_{l,x}|_0 - U_w = \ell_s \frac{\partial u_{l,x}}{\partial y}\bigg|_0, \qquad u_{r,x}|_H + U_w = -\ell_s \frac{\partial u_{r,x}}{\partial y}\bigg|_H. \tag{2.5}$$

https://doi.org/10.1017/S0022112008003649 Published online by Cambridge University Press

Finally, we have the kinetic condition of no flux across the interface:

$$\hat{n}_x u_{l,x} + \hat{n}_y u_{l,y} = \hat{n}_x u_{r,x} + \hat{n}_y u_{r,y} = 0, \tag{2.6}$$

with $\hat{n}$ the normal at the interface in $h(x)$. In the Appendix we show how to map the six boundary conditions in a closed system and solve the corresponding matrix problem as a function of the separation of scale, $\lambda = \ell_s/H$, the capillary number, $Ca = U_w \mu_l/\gamma$, and the viscosity ratio, $\chi = \mu_r/\mu_l$.

Once the pressure drop across the interface is known, one may derive using the Laplace law the equation for the local curvature, κ, of the interface:

$$\sigma \frac{\mathrm{d}\kappa}{\mathrm{d}x} = p_{r,x} - p_{l,x}, \tag{2.7}$$

with σ the surface tension at the interface. As already noticed by Jacqmin (2004), if we denote the interface arclength coordinate with s, we can consistently write with the lubrication approximation that

$$\sigma \frac{\mathrm{d}\kappa}{\mathrm{d}s} = p_{r,x} - p_{l,x}, \tag{2.8}$$

where the derivative of the curvature is connected to the angular variation $\mathrm{d}\tilde{\theta}/\mathrm{d}s = \kappa$ (where $\tilde{\theta} = \pi - \theta$). Summarizing, the governing equation set is

$$\frac{\mathrm{d}}{\mathrm{d}s}(\kappa, \tilde{\theta}, x, y) = (\sigma^{-1}(p_{r,x} - p_{l,x}), -\kappa, \cos\tilde{\theta}, -\sin\tilde{\theta}). \tag{2.9}$$

This becomes a nonlinear boundary value problem: we need to solve the ODE (ordinary differential equations) (2.9) for a given capillary number, Ca, viscosity ratio, χ, and separation of scale, $\lambda = \ell_s/H$, with the boundary conditions for the microscopic angle at the wall equal to θ_m. (For the present study we assume that the microscopic wall wettability is not dependent on the velocity.) We have therefore a four-parameter problem. To solve numerically the previous set of nonlinear ODEs, we adopt a second-order Runge–Kutta method with a non-uniform grid of increasing resolution near the wall. Notice that in the presence of two different viscosities ($\mu_r \neq \mu_l$) the interface is not symmetric with respect to the centre of the channel. For given values of viscosity ratio and capillary number, we look for solutions of (2.9) by fixing the angle in the centre of the cell, θ_M, and choosing the curvature in that location so that it matches with the desired boundary condition, θ_m.

In figure 1 we show the results for θ_M as a function of the capillary number Ca. The separation of scale is kept fixed to $\lambda = \ell_s/H = 10^{-5}$ and the viscosity ratio to $\chi = 1.0$. Various boundary conditions (i.e. microscopic wettabilities) are considered. In the limit of small Ca the macroscopic angle is equal to the microscopic wettability θ_m, but soon after Ca is increased, the interface is stretched, and the macroscopic angle decreases. By increasing the capillary number, we clearly see that there is a range in which two solutions can exist. This is typical of fixed-point structures in dynamic systems, suggesting that a bifurcation happens at a critical capillary number, Ca_{cr}, separating two branches, a stable branch ($\mathrm{d}\theta_M/\mathrm{d}Ca < 0$) and an unstable one ($\mathrm{d}\theta_M/\mathrm{d}Ca > 0$). Above the critical capillary number no stationary solution can be found: beyond this value the interface evolves dynamically, and liquid entrainment on the solid is expected to take place. To better stress the existence of a range of capillary numbers where two solutions are found we also show (see figure 2*b*) the stationary interfaces corresponding to two different outer angles, θ_M, with the same boundary physics, θ_m. From this figure we also see that our analysis

https://doi.org/10.1017/S0022112008003649 Published online by Cambridge University Press

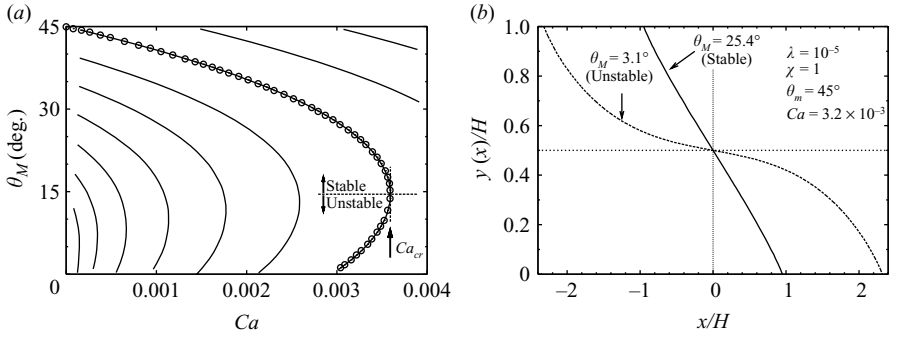


FIGURE 2. (*a*) Macroscopic angle θ_M as a function of the capillary number Ca for various microscopic angles θ_m and for a viscosity ratio $\chi = 1.0$. The value of the microscopic angle corresponding to each curve can be extracted from the small capillary number limit ($Ca \to 0$). The value of the separation of scale is kept constant at $\lambda = 10^{-5}$. Data from Jacqmin (2004) are also reported for the case with $\theta_m = 45°$ (○). On a specific curve ($\theta_m = 45°$), the critical capillary number, where the static solution becomes unstable, is indicated. (*b*) Two static profiles belonging to the stable and unstable branches for a given viscosity ratio $\chi = 1.0$. For the same microscopic contact angle ($\theta_m = 45°$) and separation of scale ($\lambda = 10^{-5}$) we show two stationary interface profiles corresponding to the same capillary number $Ca = 0.0032$. The profile is plotted in terms of dimensionless coordinates $y(x)/H$ and x/H. Results correspond to the branch shown in figure 1 where our results are compared with those of Jacqmin (2004). Notice that the unstable solutions correspond to an enlarged bending of the interface close to the wall region.

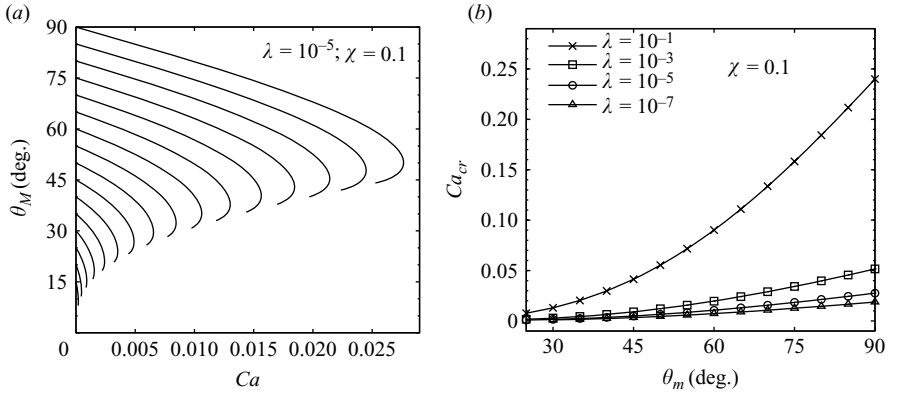


FIGURE 3. (*a*) Macroscopic angle θ_M as a function of the capillary number Ca for various microscopic angles θ_m and for a viscosity ratio $\chi = 0.1$. The value of the microscopic angle corresponding to each curve is provided by the small capillary number limit ($Ca \to 0$). The value of the separation of scale is kept constant at $\lambda = 10^{-5}$ and the viscosity ratio at $\chi = 1.0$. (*b*) The critical capillary number as a function of the microscopic angle θ_m for various separation of scales λ: $\lambda = 10^{-1}$ (×); $\lambda = 10^{-3}$ (□); $\lambda = 10^{-5}$ (○); $\lambda = 10^{-7}$ (△).

perfectly matches data presented in figure 2 of the paper by Jacqmin (2004) and reported in figure 2(*a*) using the symbols.

New results are presented for the case of a different viscosity ratio in figure 3, where we show θ_M as a function of the capillary number for a given separation of scale, $\lambda = \ell_s/H = 10^{-5}$, various microscopic wettabilities, θ_m, and fixed viscosity ratio, $\chi = 0.1$. The behaviour of the unstable branch is very sensitive to the viscosity ratio as well as the microscopic wettability: here we see that as soon as $\chi \neq 1$, the second

https://doi.org/10.1017/S0022112008003649 Published online by Cambridge University Press

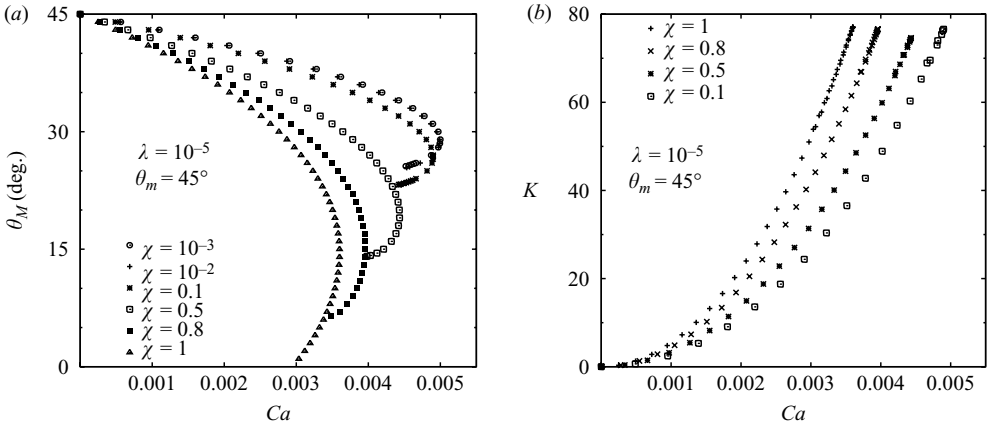


FIGURE 4. Critical capillary number as a function of the viscous ratio. (*a*) For a fixed microscopic angle ($\theta_m = 45°$) and separation of scale ($\lambda = 10^{-5}$) we show the macroscopic angle θ_M as a function of the capillary number for different viscosity ratios χ. Note the saturation of the curve when approaching values comparable with those of water and air at ordinary temperatures ($\chi \sim 0.001$). In that limit the equations are exactly solvable, and we recover the usual solution for liquid–gas film. (*b*) We plot the integral of the squared curvature along the interface $K = \int |\partial_{xx} h(x)|^2 \, \mathrm{d}x$ as a function of the capillary number for the same microscopic wettability $\theta_m = 45°$ and $\lambda = 10^{-5}$. Different viscosity ratios are chosen such as to stress the different interface stretching.

(unstable) branch no longer reaches very small values of θ_M. In figure 3(*b*) we show the critical capillary number as a function of the microscopic wettability. Notice that there are remarkable variations with respect to λ only for the larger values considered: for $\lambda = 10^{-5}$ to 10^{-7} the results are already pretty stable and weakly λ dependent. This kind of study will be important later on, when comparing with the LBE in which, because of numerical limitation, one cannot ever reach separation of scales smaller than $\lambda = 10^{-2}$ to 10^{-3}. Not surprisingly, figure 3 shows that for large-scale separation the interface becomes more stable; i.e. Ca_{cr} becomes larger.

By changing the viscosity ratio one can now understand the way Ca_{cr} is related to χ. In figure 4 we present results for θ_M as a function of Ca for a given separation of scale $\lambda = 10^{-5}$ when changing the viscosity ratio, from $\chi = 1$ down to $\chi = 10^{-3}$ (a realistic value for a liquid–gas interface at ordinary temperatures). The qualitative picture is always the same: the macroscopic angle decreases and reaches a bifurcation from which we extract the critical capillary number. We also notice that in each curve the range of macroscopic angles associated with the two branches decreases with χ and also that, on decreasing χ, we reach a limiting curve; i.e. results become almost independent of the viscosity ratio. The fact that by decreasing the viscosity ratio we increase the critical capillary number can be qualitatively understood from the equations of motion (2.1). When $\chi \to 0$ one of the two viscosities moves close to zero, whereas the other stays finite. In this limit, the contribution of the pressure gradient in the less viscous fluid becomes negligible. Therefore, the local change in the curvature given by (2.8) is triggered only by the pressure gradient of a single fluid, and we need higher capillary number to stretch it and break stationarity. This is also complemented with the integral of the squared curvature along the profile (see figure 4*a*) for the same microscopic angle and separation of scale. The increasing stretching of the interface as a function of the viscosity ratio (moving from $\chi = 0$ to $\chi = 1$) is reflected in this plot.

https://doi.org/10.1017/S0022112008003649 Published online by Cambridge University Press

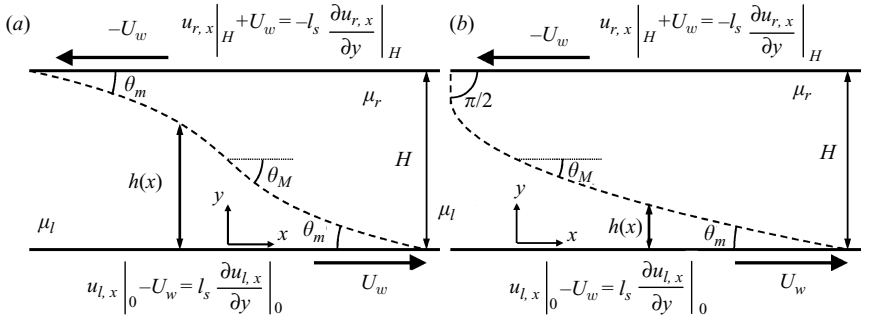


FIGURE 5. Role of the geometry. The opposite wettability configuration (*a*, configuration a) is modified into another configuration (*b*), where the top wettability is kept fixed (configuration b). In both cases we take the macroscopic angle θ_M as the angle corresponding to the location $h(x) = H/2$.

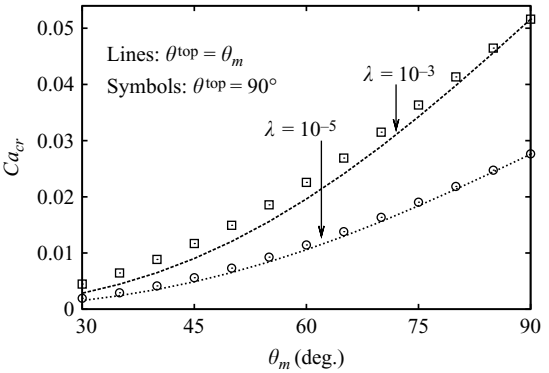


FIGURE 6. Outer scale non-universality. The critical capillary number is computed for the case of an opposite wettability boundary condition (see configuration a, figure 5) and different separations of scales (symbols). A similar analysis is done for configuration b (see figure 5), where the top wettability has been fixed to a constant value while changing only the lower wettability. The values of the separation of scales considered are between $\lambda = 10^{-5}$ and $\lambda = 10^{-3}$, and the viscous ratio is set to $\chi = 0.1$.

2.1. *Dependence on the walls' wettability*

The aim of this section is to investigate the role of the wetting boundary condition at the walls. So far, we have considered the opposite wettability boundary condition as shown in figure 1, where the angle the left liquid forms with the lower boundary is the same as the angle the right fluid forms with the upper boundary (configuration a). A possible test to understand the role of the boundary wettability is to consider another configuration (configuration b; see figure 5), where the top wettability is kept fixed to a given value. The microscopic wettability is now changed only at the lower boundary. We can compute the critical capillary number in terms of both θ_m and λ as described in the previous sections. The separation of scales considered is between $\lambda = 10^{-5}$ and $\lambda = 10^{-3}$. The critical capillary number in configuration b overestimates the case with opposite wettability (configuration a), and discrepancies are found to be enlarged when λ becomes larger (see figure 6). The separation between the two contact line regions is indeed less pronounced when λ is not very small, and differences can be expected to emerge in that limit. Overall, the discrepancies between the two

https://doi.org/10.1017/S0022112008003649 Published online by Cambridge University Press

critical capillary numbers are not that large. This is a consequence of the small values of the separation of the scale chosen. Repeating the analysis for values of $\lambda \sim 10^{-1}$ leads to a larger discrepancy, indicating that non-universality with respect to the outer geometry becomes more and more pronounced by increasing λ.

2.2. *The limit of zero viscosity ratio*

We now address the properties in the limit of zero viscosity ratio, $\chi = \mu_r/\mu_l \to 0$. To do that we have to consider only the left liquid because the other component has zero viscosity, and its pressure fluctuations are ruled out, $p_{r,x} = 0$ in (2.1). In this limit the lubrication equations simplify and reduce to the well-known treatment for liquid–gas interfaces (Eggers 2004*a*, 2005; Snoeijer 2005; Snoeijer *et al.* 2007), where viscous friction is balanced with capillary effects:

$$\frac{\mathrm{d}^3 h}{\mathrm{d}x^3} = -\frac{3Ca}{h(h+\ell_s)}. \tag{2.10}$$

This is very similar to the inner description found in a contact line problem involving the Landau–Levich geometry (Landau & Levich 1942; Derjaguin 1943) of a plate withdrawn at a given velocity from a liquid bath (Eggers 2005; Snoeijer *et al.* 2006, 2007). This inner solution is usually found by expanding in a power series in the capillary number (Voinov 1976; Hocking 1983; Eggers 2004*b*) with the final result that, away from the contact line, the cube of a macroscopic angle $\theta^3(x) \approx (\mathrm{d}h/\mathrm{d}x)^3$ changes in the manner

$$\theta^3(x) \approx \theta_m^3 - 9Ca \log\left(\frac{x}{\ell_s}\right). \tag{2.11}$$

This is basically achieved for sufficiently large arguments of x/ℓ_s, and the related range is usually called the intermediate range. When we approach Ca_{cr}, the macroscopic angle decreases, and one can argue that the relevant scaling properties of the critical capillary number can be captured by setting to zero the left-hand side of (2.11). This implies that Ca_{cr} rescales like the cube of the microscopic wettability and is inversely proportional to $\log \lambda^{-1}$. Therefore, for a fixed microscopic wettability θ_m, we expect a precise rescaling factor for the critical capillary numbers, at changes in the scale separation:

$$Ca_{cr}|_{\lambda_2} = Ca_{cr}|_{\lambda_1} \frac{\log \lambda_1}{\log \lambda_2}. \tag{2.12}$$

It is interesting to check the range of applicability of the previous heuristic argument with respect to our data. In particular, in figure 7 we check the validity of the proposed scaling relation for two characteristic viscosity ratios, $\chi = 1.0$ and $\chi = 0.1$. We consider the critical capillary number as a function of the microscopic wettability θ_m and various small separation of scales λ. We compare both unscaled and scaled critical capillary numbers using (2.12). Interestingly, we observe that the scaling behaviour is correct even for quite large θ_m, whereas the theory developed is based on a lubrication approximation in which small tilting angles are assumed (Snoeijer 2005). Notice that the scaling relation is found to also hold in the limit of equal viscosities. The term proportional to $\log \lambda$ is connected to the viscous stress divergence of the fluid at the contact line (Voinov 1976; Cox 1986; De Gennes 1986), and this happens for all the values of the viscosity ratio. Even if the equivalent of (2.11) for finite viscosity ratios is different (Cox 1986), the separation of scale always appears as $\log \lambda$, determining the main rescaling properties for the critical capillary number. In the limit of $\chi \to 0$ it is also worthwhile to compare our estimate for the critical

https://doi.org/10.1017/S0022112008003649 Published online by Cambridge University Press

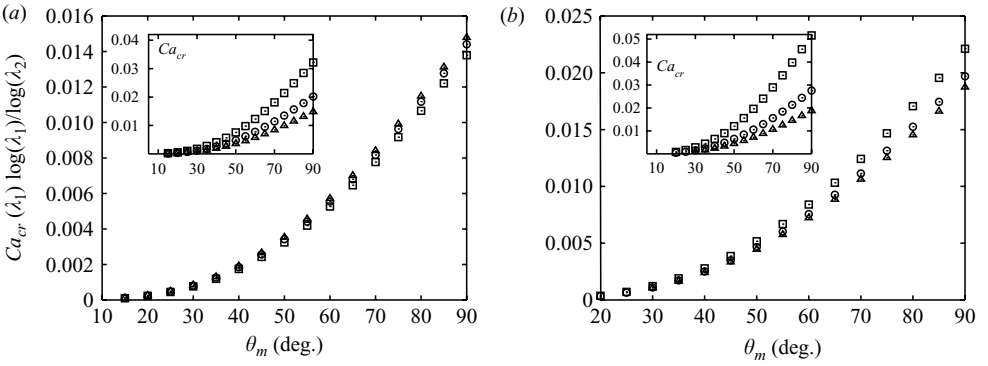


FIGURE 7. Scaling for the critical capillary number as obtained from the full hydrodynamic calculation in the lubrication approximation. (*a*) Ca_{cr} as a function of the microscopic angle θ_m for $\chi = 1.0$ is rescaled according to the formula predicted by theory. The separation of scale is kept fixed to $\lambda_2 = 10^{-7}$ ($\triangle$). Various λ_1 are then considered: $\lambda_1 = 10^{-3}$ ($\square$), $\lambda_1 = 10^{-5}$ ($\bigcirc$). In the inset we show unscaled data (same symbols) for Ca_{cr} as a function of θ_m: notice that the variability is extensively reduced for rescaled variables leading to a good collapse. (*b*) Same as (*a*) but with a viscosity ratio $\chi = 0.1$.

capillary number in the Couette cell with a similar analysis done in some recent papers (Eggers 2004*a*, 2005) for the case of the Landau–Levich geometry (Landau & Levich 1942; Derjaguin 1943) of a solid withdrawn from a liquid bath. In that case, the problem is tackled as a multi-scale problem: the inner contact line region in which viscosity is balanced with capillarity must be connected with an outer region in which gravity is balanced with capillary forces. An instability occurs when the outer meniscus approaches the shape corresponding to a perfectly wetting fluid, i.e. an apparent contact angle approaching zero degrees. An investigation of the conditions under which the highly curved contact line region can be matched to the outer profile leads to the introduction of a critical capillary number (Eggers 2004*a*, 2005)

$$Ca_{cr} = \frac{\theta_m^3}{9}\left[\log\left(\frac{Ca_{cr}^{1/3}\theta_m}{18^{1/3}\pi[\mathrm{Ai}(s_{max})]^2\lambda\theta_{in}}\right)\right]^{-1} \tag{2.13}$$

where θ_{in} is the angle of inclination of the plate with respect to the liquid bath; Ai is the Airy function; and $s_{max} = -1.0188\ldots$ is the point at which the Airy function assumes its maximum. The set-up is clearly different from a Couette cell. Nevertheless, it is useful to compare both results to understand the role of the geometry in determining the critical capillary number. We choose the same separation of scale, $\lambda = 10^{-7}$, and a small viscosity ratio, $\chi = 0.01$, in the Couette cell. This is done to determine the region in which we observe the collapse of data, as discussed in figure 4. We use two characteristic angles of inclination θ_{in} in (2.13) ($\theta_{in} = 5.73^\circ$ and $\theta_{in} = 90^\circ$), and the results are plotted in figure 8. The order of magnitude of the different critical capillary numbers is comparable, and data share the same scaling properties with respect to $\theta_m (Ca_{cr} \sim \theta_m^3)$. The presence of an overall pre-factor dependent on the geometry is clearly visible from the figure. For the sake of completeness, we have also considered a recent prediction of Hocking (2001) for fluids in narrow channels. The geometry is that of a fluid confined between two parallel plates at distance $2d$ under the effect of gravity. The main difference with the previous cases is that the speed of withdrawal is not an additional parameter, but it is fixed in terms of the bulk forcing, i.e. gravity. After introducing a Bond number $Bo = \rho_l g d^2/\sigma$, with the liquid density ρ_l and the

https://doi.org/10.1017/S0022112008003649 Published online by Cambridge University Press

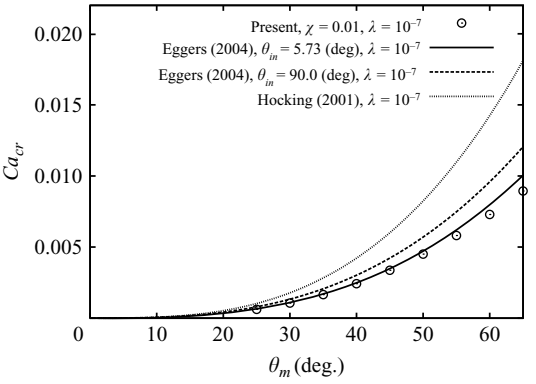


FIGURE 8. A comparison between our analysis and the proposed estimate for the critical capillary number given in (2.13) for a plate being withdrawn from a liquid at a given speed. The angle of inclination of the plate is θ_{in}, and as it emerges from Eggers (2004), the critical capillary number is a function of both the geometry and inner physics. Typical outcomes for $\theta_{in} = 5.73^\circ$ and 90° are shown. In our case we choose the same λ, and the viscosity ratio is set to a small value so as to have data already collapsed on the limiting curve for $\chi \to 0$ (figure 4). Data from Hocking (2001) are also reported for the case of a fluid in a narrow channel under the effect of gravity (equation (2.14)).

gravity g, one finds that the connection between Bo and the capillary number is $Ca = Bo/3$. In this notation μ_l is the liquid viscosity and U the average speed of motion due to gravity. A critical value in the Bond number (equation (17) in Hocking 2001) is then translated into a critical capillary number as

$$Ca_{cr} \approx \frac{0.6}{3\log(\lambda^{-1})}\theta_m^3. \tag{2.14}$$

The plot of (2.14) is also shown in figure 8 with the same λ as the previous estimates. This prediction overestimates all previous curves.

3. Numerical approach: diffuse interface methods and LBE

In this section we will use numerical simulations to further investigate the problem previously discussed. An approach based on first principles to address the inner physics of contact line problems is molecular dynamics (MD). These simulations, which usually involve Lennard–Jones liquids and several thousand molecules, appear to exhibit continuum behaviour at the macroscopic level (Koplik, Banavar & Willemsen 1989; Thompson & Robbins 1989; Barrat & Bocquet 1999; Denniston & Robbins 2001). All these MD results give insight especially in the region close to the contact line, pointing to the breakdown of the no-slip boundary condition at very small distances as a possible explanation of contact line motion (Thompson & Robbins 1989; Barrat & Bocquet 1999). Also alternative explanations of contact line motion exist, and they do not rely on the breakdown of the no-slip boundary condition. As was noticed by Seppecher (1996), a sharp interface model may be questioned. It is itself an approximation which may not be valid in the vicinity of the contact line. Molecular simulations or a continuum model need to be used to describe the interface as a diffuse layer, i.e. a layer of finite thickness. The curvature of the interface near the contact line leads to mass transport across the interface, thus removing the viscous singularity. Similar analysis in binary fluid systems (Chen, Jasnow & Vinals 2000;

https://doi.org/10.1017/S0022112008003649 Published online by Cambridge University Press

Jacqmin 2000) shows that diffusive transport of the fluid leads to effective slip at the contact line. Also mesoscopic diffuse interface models for two-phase flows based on the LBE (Wolf-Gladrow 2000; Succi 2001) have been applied to the simulation of contact line motion and related problems (Briant, Wagner & Yeomans 2004; Briant & Yeomans 2004; Jia, McLaughlin & Kontomaris 2006; Zhang & Kwok 2006; Latva-Kokko & Rothman 2007). In particular, we further elaborate along these lines, using mesoscopic diffuse interface models in which multi-phase physics is induced by using a pseudo-potential approach originally developed by Shan & Chen (1993, 1994); hereafter SC.

3.1. *LBE for non-ideal fluids*

We start from the usual LBE with a single-time relaxation (Bhatnagar, Gross & Krook 1954; Wolf-Gladrow 2000; Succi 2001):

$$f_l(\boldsymbol{x}+\boldsymbol{c}_l\Delta t, t+\Delta t) - f_l(\boldsymbol{x},t) = -\frac{\Delta t}{\tau}\left(f_l(\boldsymbol{x},t) - f_l^{(eq)}(\rho,\rho\boldsymbol{u})\right) + F_l, \qquad (3.1)$$

where $f_l(\boldsymbol{x},t)$ is the kinetic probability density function associated with a mesoscopic velocity $\boldsymbol{c}_l$ (there being a discrete set of velocities); τ is the mean collision time (with Δt a time lapse), $f_l^{(eq)}(\rho,\rho\boldsymbol{u})$ the equilibrium distribution, corresponding to the Maxwellian distribution in the continuum limit, and F_l represents a general forcing term whose role will be discussed later in the framework of inter-molecular interactions. From the kinetic distributions we can define macroscopic density and momentum fields as (Wolf-Gladrow 2000; Succi 2001):

$$\rho(\boldsymbol{x}) = \sum_l f_l(\boldsymbol{x}); \qquad \rho\boldsymbol{u}(\boldsymbol{x}) = \sum_l \boldsymbol{c}_l f_l(\boldsymbol{x}). \qquad (3.2)$$

For technical details and numerical simulations we shall refer to the nine-speed, two-dimensional 2DQ9 model (Wolf-Gladrow 2000), often used because of its numerical robustness. The equilibrium distribution in the LBEs is obtained via a low Mach number expansion of the Maxwellian continuum (Wolf-Gladrow 2000; Succi 2001):

$$f_l^{(eq)} = w_l^{(eq)}\left[\rho + \frac{c_l^i\rho u_i}{c_s^2} + \frac{\left(c_l^i c_l^j - c_s^2\delta_{ij}\right)}{2c_s^4}\rho u_i u_j\right], \qquad (3.3)$$

where $c_s^2 = 1/3$, and $i = 1, 2 = x, y$ runs over spatial dimensions. The weights $w_l^{(eq)}$ are chosen such as to enforce isotropy up to fourth-order tensor in the lattice (Wolf-Gladrow 2000; Succi 2001). From the equilibrium distribution and the symmetry properties of $\boldsymbol{c}_l$, the kinetic second-order tensor of the equilibrium distribution immediately follows (Wolf-Gladrow 2000):

$$\sum_l f_l^{(eq)} c_l^i c_l^j = \delta_{ij}\left(c_s^2\rho\right) + \rho u_i u_j,$$

where, in the first term of the right-hand side, we recognize the ideal-gas pressure tensor $P_{ij} = \delta_{ij}(c_s^2\rho)$. In order to study non-ideal effects we need to supplement the previous description with an inter-particle forcing. This is done by choosing a suitable F_l in (3.1). In the original SC model, the bulk inter-particle interaction is proportional to a free parameter (the ratio of potential to thermal energy) $\mathscr{G}_b$, entering the equation for the momentum balance:

$$F_i = \sum_l F_l c_l^i = -\mathscr{G}_b c_s^2 \sum_l w(|\boldsymbol{c}_l|^2)\psi(\boldsymbol{x},t)\psi(\boldsymbol{x}+\boldsymbol{c}_l\Delta t, t)c_l^i, \qquad (3.4)$$

https://doi.org/10.1017/S0022112008003649 Published online by Cambridge University Press

where $w(|\boldsymbol{c}_l|^2)$ is the static weights and $\psi(\boldsymbol{x},t)=\psi(\rho(\boldsymbol{x},t)$ is the (pseudo-) potential function which describes the fluid–fluid interactions triggered by inhomogeneities of the density profile (Wolf-Gladrow 2000; Sbragaglia *et al.* 2007). We shall refer to the pseudo-potential used in the original SC work, namely

$$\psi(\boldsymbol{x},t)=(1-\exp(-\rho(\boldsymbol{x},t))). \tag{3.5}$$

Note that this reduces to the correct form $\psi\to\rho$ in the limit $\rho\ll 1$, whereas at high density ($\rho\gg 1$), it shows a saturation. The latter is crucial to prevent density collapse of the high-density phases. (The SC potential is purely attractive, so a mechanism stabilizing the high-density phase is mandatory to prevent density collapse.) In principle, other functional forms may be investigated, sometimes with impressive enhancement of the density ratios supported by the model (Yuan & Schaefer 2006).

In order to understand the corrections to the ideal-state equation induced by the pseudo-potential, we need to define a consistent pressure tensor P_{ij} for the macroscopic variables:

$$\partial_j P_{ij}=-F_i+\partial_i\left(c_s^2\rho\right). \tag{3.6}$$

Upon Taylor expansion of the forcing term and assuming hereafter $\Delta t=1$, we obtain

$$F_i=-\mathscr{G}_b c_s^2\psi\partial_i\psi-\frac{\mathscr{G}_b}{2}c_s^4\psi\partial_i\Delta\psi, \tag{3.7}$$

which is correctly translated (He & Doolen 2002; Benzi *et al.* 2006) into

$$P_{ij}=\left(c_s^2\rho+\mathscr{G}_b\frac{c_s^2}{2}\psi^2+\mathscr{G}_b\frac{c_s^4}{4}|\nabla\psi|^2+\mathscr{G}_b\frac{c_s^4}{2}\psi\Delta\psi\right)\delta_{ij}-\frac{1}{2}\mathscr{G}_b c_s^4\partial_i\psi\partial_j\psi. \tag{3.8}$$

The evolution scheme (3.1) together with the inter-particle force (3.4) approximates the following diffuse interface equations for the density and momentum fields (3.2):

$$\partial_t\rho+\partial_j(\rho u_j)=0, \tag{3.9}$$

$$\partial_t(\rho u_i)+u_j\partial_j(\rho u_i)=-\partial_j P_{ij}+\partial_j\Pi_{ij} \tag{3.10}$$

with Π_{ij} the usual viscous stress tensor (Wolf-Gladrow 2000; Succi 2001; Briant *et al.* 2004; Briant & Yeomans 2004). Capillary effects, mimicking non-trivial interactions with the wall, can be incorporated in this approach by using a suitable wall function (Sbragaglia *et al.* 2006, 2007).

A disadvantage of the SC formulation is that, there being only one free parameter to tune ($\mathscr{G}_b$), one cannot independently change the density ratio and surface tension. Here we use a recent extension of the SC model that overcomes this limitation, by introducing first and second neighbours coupling in the pseudo-potential (Sbragaglia *et al.* 2007):

$$F_i=-c_s^2\sum_l w(|\boldsymbol{c}_l|^2)\psi(\boldsymbol{x},t)[\mathscr{G}_1\psi(\boldsymbol{x}+\boldsymbol{c}_l,t)+\mathscr{G}_2\psi(\boldsymbol{x}+2\boldsymbol{c}_l,t)]c_l^i. \tag{3.11}$$

This coupling leads to the following pressure tensor in the continuum limit:

$$P_{ij}=\left(c_s^2\rho+(\mathscr{G}_1+2\mathscr{G}_2)\frac{c_s^2}{2}\psi^2+(\mathscr{G}_1+8\mathscr{G}_2)\left(\frac{c_s^4}{4}|\nabla\psi|^2+\frac{c_s^4}{2}\psi\Delta\psi\right)\right)\times\delta_{ij}-\frac{(\mathscr{G}_1+8\mathscr{G}_2)}{2}c_s^4\partial_i\psi\partial_j\psi. \tag{3.12}$$

Furthermore, in order to reduce the importance of spurious currents at interfaces (Cristea & Sofonea 2003; Wagner 2003; Lee & Fischer 2006; Shan 2006; Yuan &

https://doi.org/10.1017/S0022112008003649 Published online by Cambridge University Press

Schaefer 2006; Sbragaglia *et al.* 2007) one can also introduce the non-ideal terms directly into the equilibrium distribution as explained in some recent papers (Briant *et al.* 2004; Briant & Yeomans 2004). With this strategy we impose the desired pressure tensor instead of writing explicitly the forcing term (3.11). We can thus use $\mathscr{G}_1$ and $\mathscr{G}_2$ to vary the density ratio and width of the interface (i.e. surface tension) independently. As a matter of fact, the use of Van der Waals pressure tensors (Briant *et al.* 2004; Briant & Yeomans 2004) may limit seriously the density ratios achieved in the simulations.

3.2. *Stationary contact line description: Cox (1986) vs LBE*

In this sub-section we explore and investigate the conditions under which our diffuse interface models converge with the predictions of sharp interface hydrodynamics. As we have already seen and discussed in (2.11), we should expect an intermediate range with a prediction of scaling for the slope of the interface in terms of the capillary number and microscopic slip length. A further extension for that prediction of scaling for two fluids with finite viscosity ratio has been provided by Cox (1986). This scaling relation translates (see figure 1 in Cox 1986) in our coordinates (see figure 1) as

$$g(\theta(r), \chi) = g(\theta(0), \chi) + Ca_g \log(r/\ell_s), \tag{3.13}$$

$$g(\theta, \chi) = \int_0^\theta \frac{1}{f(x, \chi)} \mathrm{d}x \tag{3.14}$$

and

$$f(x, \chi) = \frac{2 \sin x [\chi^{-2}(x^2 - \sin^2 x) + 2\chi^{-1}(x(\pi - x) + \sin^2 x) + ((\pi - x)^2 - \sin^2 x)]}{\chi^{-1}(x^2 - \sin^2 x)((\pi - x) + \sin x \cos x) + ((\pi - x)^2 - \sin^2 x)(x - \sin x \cos x)}, \tag{3.15}$$

where we have defined $Ca_g = \mu_r U_w/\sigma$ as the capillary number estimated in the less viscous fluid, r as the distance from the stationary contact line and the angle $\theta(r)$ consistent with the notation of figure 1 in Cox (1986). The paper by Cox studies a pure sharp interface treatment of the moving contact line, involving a finite viscosity ratio and the length scale ℓ_s associated with microscopic slip motion. This approach turns out to be extremely useful to compare with simulations, where it is difficult to reach very small viscous ratios. We expect that in diffuse interface methods, when we look at the contact line on scales much larger than the interface width ξ, a quantitative matching with the sharp interface prediction (3.13) is recovered. The length scale ℓ_s is now associated with the effective slip generated by the diffuse interface mechanisms (Seppecher 1996; Jacqmin 2000; Pismen & Pomeau 2000). This study opens the possibility of testing the universality in the intermediate region independent of the inner physics mechanisms. In our numerical simulations we fix the viscosity ratio $\chi = 0.1$, and the associated density ratio is so chosen that the interface width ξ is of the order of some grid points. (One would need a systematic procedure to give ξ. A possible way is to define ξ in terms of those points on which the local gradient exceeds a given threshold. In any case the width ξ does not exceeds some units, and it is reassuring to assume $\xi/\Delta x = 4 \pm 1$ for the case of $\chi = 0.1$.) The wetting properties are chosen as explained in some recent studies (Benzi *et al.* 2006; Sbragaglia *et al.* 2007). In particular, for the present set of simulations, we use a neutral wetting boundary condition, $\theta(0) = \pi/2$ in (3.13). To do that we assume that the pseudo-potential of the lattice Boltzmann description (3.5) achieves a neutral stress at the boundaries ($\partial_n \psi = 0$, with n the normal with respect to the wall). With a fixed Ca_g, interface width ξ and

https://doi.org/10.1017/S0022112008003649 Published online by Cambridge University Press

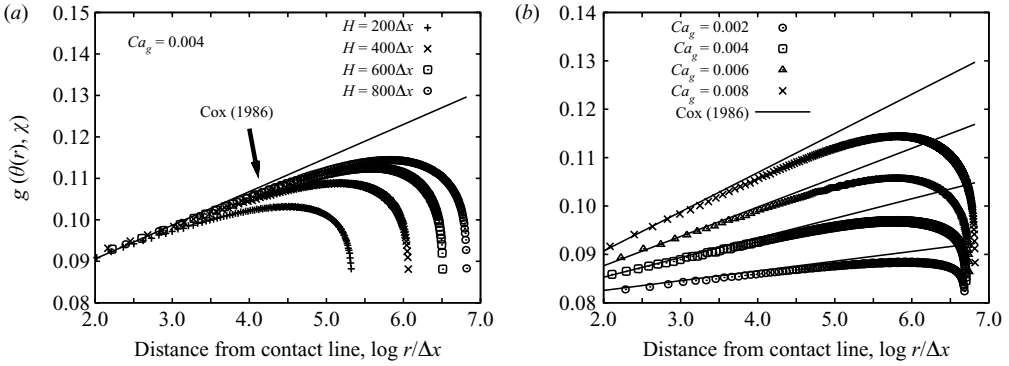


FIGURE 9. The comparison between numerical simulations and the scaling relations for the intermediate region as predicted by Cox (1986). (*a*) The scaling for $g(\theta, \chi)$ as a function of the distance from the contact line r. For a fixed capillary number in the gas phase, Ca_g, fixed viscosity ratio, χ, and fixed slip length, the sharp interface theory predicts a linear scaling of the function $g(\theta, \chi)$ (see (3.13)) with respect to $\log r$. The development of the intermediate region is shown for various numerical resolutions approaching the sharp interface limit, where theory and numerics become asymptotically comparable. In the intermediate region the slope is the one predicted by theory, i.e. equal to $Ca_g = \mu_r U_w/\sigma$. (*b*) Same as (*a*) with different capillary numbers and a given resolution in the vertical direction.

viscosity ratio $\chi = 0.1$ we then carry out numerical simulations in our Couette cell by increasing the distance between the walls: $H = 200\Delta x, 400\Delta x, 600\Delta x, 800\Delta x$ (see figure 9*a*), with Δx the lattice spacing. Half of the computational domain is then initialized with the left, more viscous fluid, and rotational boundary conditions are implemented at the inlet and outlet as discussed by Briant & Yeomans (2004). No-slip boundary conditions are implemented exactly; i.e. the mechanism of removing the contact line singularity is found in compressibility effects because of the diffuse nature of the model. The results of the numerical simulations (see figure 9) clearly show that by enlarging the resolution, i.e. increasing the ratio of the outer scale H with respect to the interface width, we correctly approach the linear scaling behaviour of $g(\theta(r), \chi)$ with respect to $\log r$. The slope is correctly given by Ca_g in (3.13). The linearity with respect to Ca_g is further checked in figure 9(*b*), where we keep H fixed and simply change the capillary number by changing the velocity at the wall U_w.

3.3. *Full hydrodynamic calculations: lubrication theory vs LBE*

In the previous sub-section we quantitatively matched the diffuse interface methods with the universal scaling properties in the intermediate range, as predicted by Cox (1986). To achieve a good comparison, a lattice Boltzmann separation of scale, $\lambda_{LBE} = \xi/H$, must be chosen as a small-scale parameter; i.e. the scales of observation must be larger with respect to the inner length scale specified by the interface width ξ. Clearly, λ_{LBE} plays the role of the separation of scale in the diffuse interface description. In particular, we can investigate the possibility of a quantitative matching with the prediction from the full hydrodynamical calculation developed in the first part of the paper. By doing so, we are able to explore the comparison between the two descriptions (sharp vs diffuse) on all length scales and not simply in the intermediate range as done in the previous sub-section. To do that we choose the same viscosity ratio as before ($\chi = 0.1$), and we fix the distance between the walls to be $H = 100\Delta x$. The microscopic wettability θ_m is chosen to be equal to 58°, and then we vary the capillary number Ca. For each value of Ca we reach the stationary state

https://doi.org/10.1017/S0022112008003649 Published online by Cambridge University Press

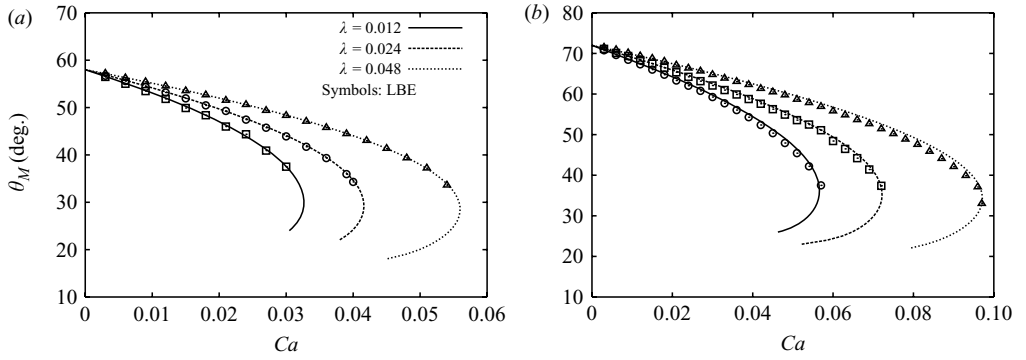


FIGURE 10. The comparison between theory and numerical simulations for the macroscopic angle θ_M as a function of the capillary number Ca on the stable branch. (a) For a fixed microscopic angle $\theta_m = 58°$, three different scale separations λ are used: $\lambda = 0.048$ ($\triangle$); $\lambda = 0.024$ ($\bigcirc$); $\lambda = 0.012$ ($\square$). In the numerics the different scale separations are obtained by fixing the interface width in the diffuse interface approach and using different heights H. (b) Same as (a) for a microscopic contact angle $\theta_m = 72°$.

and obtain the corresponding value of the angle in the centre of the cell (θ_M). To extract the angle we perform a contour plot of the density field on the interface at the level $\rho_{av} = (\rho_g + \rho_l)/2$, with ρ_g and ρ_l the gas and liquid densities, respectively. The corresponding plot of θ_M vs Ca is shown in figure 10(a). Notice that when we reach a critical value of the capillary number, no stationary interface is observed above that value. This is precisely the same behaviour as predicted by theory. In particular, we can find the correct value of λ in the sharp interface treatment of the Couette cell able to fit correctly the numerical prediction. It is found that the correct value of λ is approximately 0.024, which is of the order of λ_{LBE}. We can also repeat the whole experiment with the viscosity ratio and interface width fixed to the same values but doubling or reducing by a factor 2 the resolution between the walls. We expect (as observed in figure 10) that the corresponding numerical data would match with the theoretical prediction obtained by doubling or reducing by a factor 2 the previously used λ. The same study is also done with a different microscopic wettability ($\theta_m = 72°$; see figure 10b). Overall, we observe a good agreement between the two approaches.

In figure 11 we compare stationary interface profiles for a fixed viscosity ratio, $\chi = 0.1$, and two characteristic capillary numbers, $Ca = 0.022$ and $Ca = 0.033$. We choose $H = 100\Delta x$, and the interface width ξ is kept fixed. The corresponding prediction from the theory has been produced with the value of λ that matches the corresponding numerics in the plot of θ_M as a function of Ca (see middle plots of figure 10). It should be noticed that the bulk regions are correctly matched, whereas small discrepancies emerge close to the boundaries. One may want to argue that the lubrication theory is valid only in the limit of small tilting angles (i.e. microscopic wettabilities), and the presence of finite wettabilities can produce a small mismatch between theory and numerics. However, it should also be noted that close to the boundaries the inner physics is completely different: in the sharp interface limit the dynamics is dominated by slip properties while in the diffuse interface case by the finite thickness of the interface. Overall, at least for the range of parameters studied here, the agreement is satisfactory and shows a good global universality with respect to the mechanisms resolving the contact line singularity.

Much more stringent comparisons can be carried out by looking at the local details in the stationary regime of the velocity field. Numerical and theoretical snapshots of

https://doi.org/10.1017/S0022112008003649 Published online by Cambridge University Press

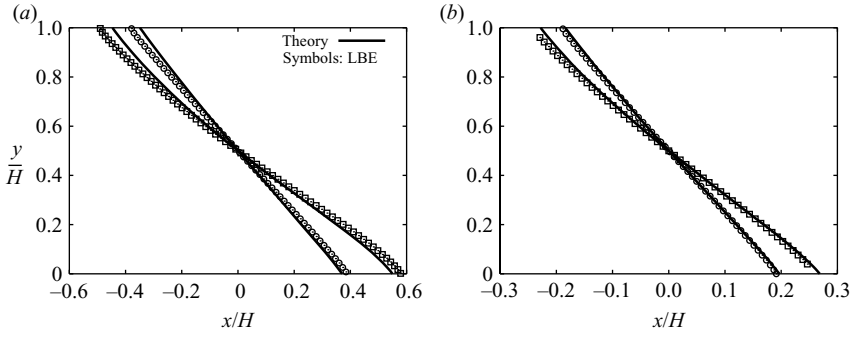


FIGURE 11. The static interface shape for a given capillary number and microscopic angle θ_m. (*a*) For $\theta_m = 58^\circ$ we show the results of the numerical simulations for two different capillary numbers: $Ca = 0.033$ (□), $Ca = 0.012$ (○). The corresponding theoretical prediction is shown (—). The horizontal and vertical coordinates have been made dimensionless with respect to the system's height H. The separation of scale λ in the theory is 0.024, i.e. the correct one to reproduce the diffuse interface results for the macroscopic angle θ_M as a function of the capillary number Ca (see figure 10). (*b*) Same as (*a*) but for $\theta_m = 72^\circ$.

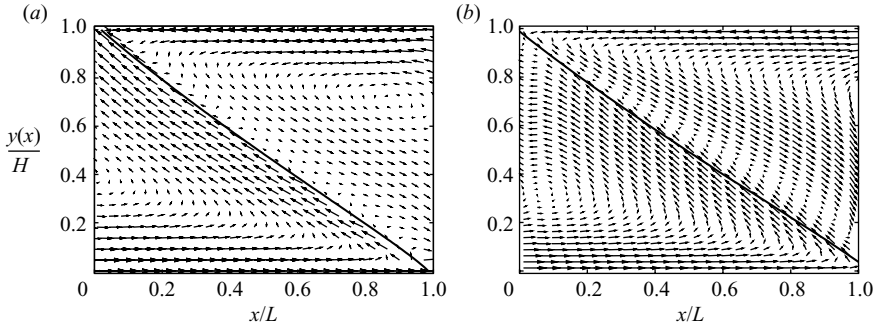


FIGURE 12. A stationary state of the Couette cell in the numerics with diffuse interface (*a*) and in the sharp interface theory (*b*). The vertical length scale has been made dimensionless with respect to the height H and the horizontal one with respect to the horizontal extent of the interface L. Good agreement is found in the qualitative details of the velocity fields: a two-roll structure is developed in both the gas and liquid phases. These plots share qualitative features with the molecular dynamics simulations by Thompson & Robbins (1989). The interface location is also displayed (lines angling from wall to wall).

the velocity vector are displayed in figure 12. Qualitative features are very similar for both cases. In fact, it is evident from both theory and numerics that a two-roll structure (Thompson & Robbins 1989) is present in the two fluids. Looking at the details of the velocity field in the streamwise (x) direction we can further compare theory and numerics. In figure 13(*b*), for a fixed capillary number Ca, viscosity ratio χ, separation of scale λ and microscopic wettability θ_m, we show the streamwise component of the velocity ($u_x(x, y)$) as a function of y for various horizontal locations x, as extracted from the theory developed in § 2 . Further details in terms of the separation of scales λ are displayed in figure 13(*b*). When we fix the parameters Ca, χ and θ_m, the velocity profiles tend to converge with the master plot for small values of λ.

It is interesting to carry out a similar analysis in the numerics. To do that, we can fix the viscosity ratio χ, the microscopic wettability θ_m and the capillary number Ca to be the same as the case of figure 13(*b*). With the interface width ξ fixed to a

https://doi.org/10.1017/S0022112008003649 Published online by Cambridge University Press

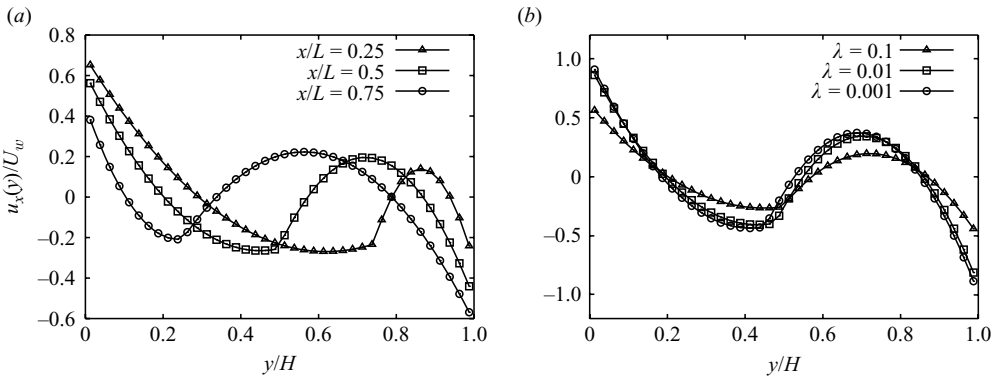


FIGURE 13. Velocity profiles in the streamwise direction as obtained from theory. (*a*) Velocity field $u_x(x, y)$ as a function of y/H for different values of x along the horizontal direction (see also figure 12) of the interface L: $x/L = 0.25$ (△); $x/L = 0.5$ (□); $x/L = 0.75$ (○). The separation of scale is $\lambda = 0.1$; the capillary number is $Ca = 0.011$; and the microscopic angle is $\theta_m = 58°$. (*b*) The velocity profiles in the streamwise direction $u_x(x, y)$ as functions of y/H, for $x/L = 0.5$ and different separations of scales: $\lambda = 0.1$ (△); $\lambda = 0.01$ (□); $\lambda = 0.001$ (○).

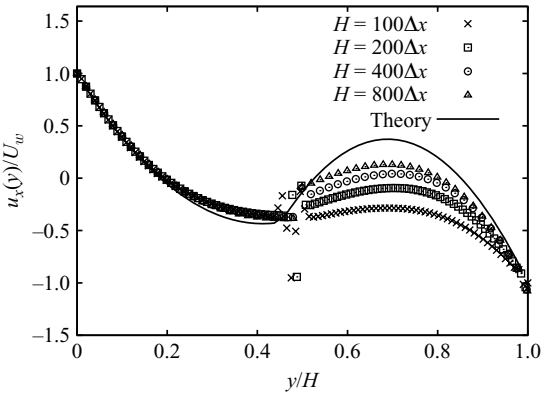


FIGURE 14. Comparison between theory and numerical simulations. We show the velocity field in the streamwise direction $u_x(x, y)$ as a function of y/H, for $x/L = 0.5$ (L is the horizontal length scale of the interface, see also figure 12), for a capillary number $Ca = 0.011$ and a microscopic angle $\theta_m = 58°$. The theoretical profile is obtained with a separation of scale $\lambda = 0.001$, already in the region of saturation shown in figure 13. The numerical results are obtained with a fixed interface width ξ and increasing numerical resolution in the vertical direction, i.e. at decreasing the separation of scale $\lambda_{LBE} = \xi/H$.

given value, we can then increase the resolution between the walls and study the way the diffuse interface velocity converges with the sharp interface prediction. Results are presented in figure 14. We notice that by increasing the resolution H from $100\Delta x$ to $800\Delta x$, by $H = 600\Delta x$ we have already reached a limiting profile. On the other hand, if we compare the asymptotic numerical profile with the theoretical prediction (solid line in figure 14) we observe a mismatch in the less viscous region. The discrepancy can be due to different factors. First, we can argue that the sharp interface prediction coming from the lubrication theory may not be fully correct for finite wettabilities; i.e. a small overestimation in the pressure gradients would be amplified in the less viscous part as predicted by the stationary Stokes equations (2.1). It should be possible to clarify

https://doi.org/10.1017/S0022112008003649 Published online by Cambridge University Press

this point using a full two-dimensional calculation, as for example the one discussed by Somalinga & Bose (2000). Second, one should notice that in the interface region spurious effects emerge in the numerics. This is due to the presence of a stretched interface with local gradients in the density field (Yuan & Schaefer 2006; Sbragaglia *et al.* 2007). Neverthless, the comparison of the shape of the interfaces between LBE and the sharp interface hydrodynamics did not reveal a great mismatch (see figures 9–11); i.e. regarding this point the effect of spurious currents is certainly small. In order to make progress on this issue, one should work out a better and refined numerical scheme to reduce the spurious currents effect and check the comparison with theory again (Cristea & Sofonea 2003; Wagner 2003; Lee & Fischer 2006; Shan 2006; Yuan & Schaefer 2006; Sbragaglia *et al.* 2007).

4. Discussions and conclusions

We have developed a sharp interface theory to describe a Couette cell consisting of two immiscible fluids. The two contact lines at the walls develop divergent viscous stresses, and such a singularity is removed by introducing a finite slip length at the boundaries (ℓ_s). The stationary properties of the system have been quantified in terms of the capillary number (Ca), the viscosity ratio (χ), the microscopic wettability (θ_m) and the separation of scale (λ) between the inner physics (ℓ_s) and the outer geometry (i.e. the distance between the walls H). The problem can be closed using the assumption of small tilting angles at the interface (lubrication approximation), thus determining the stationary interfaces in terms of Ca, χ, θ_m and λ. It is observed that there exists a critical capillary number, Ca_{cr}, above which no stationary solution can be found. The critical capillary number corresponds to the case in which liquid deposition occurs on the solid: the interface is stretched to the point beyond which it cannot sustain any longer a stationary profile and it is broken in favour of liquid entrainment on the wall. Our analysis offers the possibility to examine this critical capillary number in terms of all parameters, especially the viscosity ratio, thus extending a similar analysis done in a recent paper by Jacqmin (2004). Moreover, in the limit of small viscosity ratios, it allows our results to be compared with the recent analysis proposed by Eggers (2004*a*) for the case of a plate withdrawn at a given speed from a liquid bath. This elucidates the role of completely different geometries in determining the critical capillary numbers.

In the second part of the paper we have studied the same system with a diffuse interface model based on the LBE. The comparison with LBE results allows us to consider the numerical model as the benchmark and to understand the effects of finite thickness of the interface on global quantities, such as the critical capillary number, as well as local ones, such as the interface shape and the velocity profiles. Good agreement is found when the scale separation in LBE, given by the ratio of interface thickness ξ and distance between the walls H, becomes small enough.

Extensions of LBE simulations to other geometries, as seen in the Landau–Levich case in the presence of gravity, would allow direct comparison with experimental results (Quéré 1991; Snoeijer *et al.* 2006, 2007) and also offer more physical insight into problems that are still not completely understood, such as the importance of roughness, contact angle hysteresis and speed dependency of the microscopic wetting properties (Quéré 1991; Golestanian & Raphael 2003; Heine, Grest & Webb 2004; Rame, Garoff & Willson 2004).

Very recently, a withdrawal experiment by Snoeijer *et al.* (2006) has been performed and, contrary to previous experiments (Sedev & Petrov 1991), the transition to film entrainment did not occur at the critical capillary number predicted by the theory

https://doi.org/10.1017/S0022112008003649 Published online by Cambridge University Press

(Eggers 2004*a*, 2005). This behaviour is due to the formation of a capillary ridge that does not trivially match the liquid film and determines the critical speed of entrainment. This can be related to contact angle hysteresis that has not been treated in the continuum models; the sensitivity of Ca_{cr} with respect to θ_m (see also figure 3) can also support this interpretation. Another interesting possibility would be the introduction of a mesoscopic roughness in the numerical simulations and studying the way this critical behaviour changes in terms of the underlying heterogeneity (Kusumaatmaja & Yeomans 2007). One should be cautioned that such an analysis would be limited to finite viscosity ratios, unless one is opting for more sophisticated schemes incorporating density ratios comparable with liquid–gas interfaces used in the experiments (Inamuro *et al.* 2004; Lee & Lin 2005). Moreover, the properties of the diffuse interface models will emerge as functions of the separation of scale λ_{LBE}: reaching extremely small values of λ_{LBE} is somewhat prohibitive because of the extremely large resolution needed to simulate a set of scales ranging from nm to tens of μm. In this regard, analysis similar to that presented in this paper (see § 2.2) would help to translate the numerical observations into realistic numbers.

We are indebted to B. Andreotti, R. Benzi, J. Yeomans, H. Kusumaatmaja, F. Toschi and S. Succi for useful and enlightening discussions.

Appendix. Matrix problem for the lubrication approximation

Here we describe in detail the calculations needed to solve the Couette problem in the lubrication approximation. Consistent with the assumption of small tilting angles, the vector normal to the interface is

$$\hat{n} = \frac{1}{\sqrt{1 + (\mathrm{d}h/\mathrm{d}x)^2}} \left(\hat{e}_y - \hat{e}_x \frac{\mathrm{d}h}{\mathrm{d}x} \right) \tag{A 1}$$

with $\hat{e}_x$ and $\hat{e}_y$ being Cartesian unit vectors. A zero-normal component for the left field (similar arguments being applicable to the right one) at the interface means

$$u_{l,n}|_h = u_{y,l}|_h - \frac{\mathrm{d}h}{\mathrm{d}x}\, u_{x,l}|_h = 0. \tag{A 2}$$

Moreover from the continuity equation (2.2) we derive

$$u_{y,l}|_h = -\frac{\mathrm{d}}{\mathrm{d}x} \int_0^{h(x)} u_{x,l} \mathrm{d}y + \frac{\mathrm{d}h}{\mathrm{d}x}\, u_{x,l}|_h \,. \tag{A 3}$$

The use of (A 3) together with (A 2) leads to

$$u_{l,n}|_h = \frac{\mathrm{d}}{\mathrm{d}x} \int_0^{h(x)} u_{x,l} \mathrm{d}y. \tag{A 4}$$

Since in the inner (outer) region of the system there is no net mass flow rate

$$\int_0^{h(x)} u_{x,l} \mathrm{d}y = 0 \qquad \int_{h(x)}^{H} u_{x,r} \mathrm{d}y = 0. \tag{A 5}$$

The six boundary conditions that we need to fix A_l, B_l, $p_{l,x}$, A_r, B_r, $p_{l,x}$ are then represented by (2.4), (2.5) and (A 5). They translate to the following system:

$$A_l + hB_l + \frac{h^2}{2} p_{l,x} - \chi^{-1} \left(A_r + hB_r + \frac{h^2}{2} p_{r,x} \right) = 0; \tag{A 6}$$

https://doi.org/10.1017/S0022112008003649 Published online by Cambridge University Press

$$B_l + hp_{l,x} - B_r - hp_{r,x} = 0; \tag{A 7}$$

$$A_l - \ell_s B_l = \mu_l U_w; \tag{A 8}$$

$$A_r + (H + \ell_s)B_r + \left(\frac{H^2}{2} + \ell_s H\right) p_{r,x} = -\mu_r U_w; \tag{A 9}$$

$$hA_l + \frac{h^2}{2}B_l + \frac{h^3}{6}p_{l,x} = 0; \tag{A 10}$$

$$(H - h)A_r + \frac{1}{2}(H^2 - h^2)B_r + \frac{1}{6}(H^3 - h^3)p_{r,x} = 0. \tag{A 11}$$

REFERENCES

Barrat, J.-L. and Bocquet, L. 1999 Influence of wetting properties on hydrodynamic boundary conditions at a fluid/solid interface. *Faraday Discuss.* **112**, 119–127.

Benzi, R., Biferale, L., Sbragaglia, M., Succi, S. & Toschi, F. 2006 Mesoscopic modeling of a two-phase flow in the presence of the boundaries: the contact angle. *Phys. Rev.* E **74**, 021509.

Blake, T. D. 2006 The physics of moving wetting lines. *J. Colloid Interface Sci.* **299**, 1–13.

Blake, T. D. & Ruschak, K. J. 1979 A maximum speed of wetting. *Nature* **282**, 489–491.

Bhatnagar, P. L., Gross, E. & Krook, M. 1954 A model for collision processes in gases. *Phys. Rev.* **94**, 511–525.

Briant, A. J., Wagner, A. J. & Yeomans, J. M. 2004 Lattice Boltzmann simulations of contact line motion: I; liquid–gas systems. *Phys. Rev.* E **69**, 031602.

Briant, A. J. & Yeomans, J. M. 2004 Lattice Boltzmann simulations of contact line motion: II; binary fluids. *Phys. Rev.* E **69**, 031603.

Cox, R. G. 1986 The dynamic of the spreading of liquids on a solid surface. *J. Fluid Mech.* **168**, 169–194.

Chen, H. Y., Jasnow, D. & Vinals, J. 2000 Interface and contact line motion in a two phase fluid under shear flow. *Phys. Rev. Lett.* **85**, 1686.

Cristea, A. & Sofonea, V. 2003 Reduction of spurious velocity in finite difference lattice Boltzmann models for liquid–vapor systems. *Intl J. Mod. Phys.* **14**, 1251–1266.

De Gennes, P. G. 1985 Wetting: statics and dynamics. *Rev. Mod. Phys.* **57**, 827–863.

De Gennes, P. G. 1986 Deposition of Langmuir–Blodget layers. *Colloid Polymer Sci.* **264**, 463–465.

Denniston, C. & Robbins, M. O. 2001 Molecular and continuum boundary conditions for a miscible binary fluid. *Phys. Rev. Lett.* **87**, 178302.

Derjaguin, B. V. 1943 On the thickness of a layer of liquid remaining on the walls of vessels after their emptying, and the theory of the application of photoemulsion after coating on the cone film. *Acta Physichochim. URSS* **20**, 349.

Ding, H. & Spelt, P. D. M. 2007 Inertial effects in droplet spreading: a comparison between diffuse-interface and level-set simulations. *J. Fluid. Mech.* **576**, 287–296.

Dussan, E. B. V. 1979 Spreading of liquids on solid surfaces – static and dynamic contact lines. *Annu. Rev. Fluid Mech.* **11**, 371–400.

Dussan, E. B. V., Rame, E. & Garoff, S. 1991 On identifying the appropriate boundary conditions at moving contact lines. An experimental investigation. *J. Fluid Mech*, **230** 97–116.

Eggers, J. 2004*a* Hydrodinamic theory of forced dewetting. *Phys. Rev. Lett.* **93**, 094502.

Eggers, J. 2004*b* Towards a description of contact line motion at higher capillary numbers. *Phys. Fluids* **16**, 3491.

Eggers, J. 2005 Existence of receding and advancing contact lines. *Phys. Fluids* **17**, 082106.

Ghannum, M. T. & Esmail, M. N. 1993 experimental study of the wetting of fibers. *AIChe J.* **39**, 361–365.

Golestanian, R. and Raphael, E. 2001*a* Dissipation in dynamics of a moving contact line. *Phys. Rev.* E **64**, 031601.

Golestanian, R. & Raphael, E. 2001*b* Relaxation of a moving contact line and the Landau-Levich effect. *Europhys. Lett.* **55**, 228–234.

https://doi.org/10.1017/S0022112008003649 Published online by Cambridge University Press

Golestanian, R. & Raphael, E. 2003 Roughening transition in a moving contact line. *Phys. Rev.* E **67**, 031603.

He, X. and Doolen, G. 2002 Thermodynamic foundations of kinetic theory and lattice Boltzmann models for multiphase flows. *J. Stat. Phys.* **107**, 309–328.

Heine, D. R., Grest, G. S. & Webb, E. B. 2004 Spreading dynamics of polyer nanodroplets in cilindrical geometries. *Phys. Rev.* E **70**, 011606.

Hocking, L. M. 1983 The spreading of a thin drop by gravity and capillarity. *Q. J. Mech. Appl. Math.* **36**, 55–69.

Hocking, L. M. 2001 Meniscus draw-up and draining. *Euro. J. Appl. Maths.* **12**, 195–208.

Hocking, L. M. & Rivers, A. D. 1982 The spreading of a drop by capillary action. *J. Fluid Mech.* **121**, 425–442.

Huh, C. & Scriven, L. E. 1971 Hydrodynamics model of steady movement of a solid/liquid/fluid contact line. *J. Colloid Interface Sci.* **35**, 85–101.

Inamuro, T., Ogata, T., Tajima, S. & Konishi, N. 2004 A lattice Boltzmann method for incompressible two-phase flows with large density differences. *J. Comp. Physics* **198**, 628–644.

Jacqmin, D. 2000 Contact-line dynamics of a diffuse fluid interface. *J. Fluid. Mech* **402**, 57–88.

Jacqmin, D. 2004 Onset of wetting failure in liquid-liquid systems. *J. Fluid. Mech.* **517**, 209–228.

Jia, X., Mc Laughlin, J. B. & Kontomaris, 2006 Lattice Boltzmann simulations of contact line motion on uniform surfaces. *Math. Comp. Sim.* **72**, 156–159.

Kistler, S. F. 1993 Hydrodynamics of wetting. In *Wettability* (ed. J. Berg), pp. 311–429. Marcel Dekker.

Koplik, J., Banavar, J. R. & Willemsen, J. F. 1989 Moleculer dynamics of fluid flow at solid surfaces. *Phys. Fluids* A **1**, 781.

Kusumaatmaja, H. & Yeomans, J. M. 2007 Modelling contact angle hysteresis on chemically patterned and superhydrophobic surfaces. *Langmuir* **23**, 6019–6032.

Landau, L. D. & Levich, B. V. 1942 Dragging of a liquid by a moving plate. *Acta Physicochimica URSS* **17**, 42.

Latva-Kokko, M. & Rothman, D. H. 2007 Scaling of dynamic contact angles in a lattice Boltzmann model. *Phys. Rev. Lett.* **98**, 254503.

Lee, T. & Fischer, P. F. 2006 Eliminating parasitic currents in the lattice Boltzmann equation method for nonideal gases. *Phys. Rev.* E **74**, 046709.

Lee, T. & Lin, C.-L. 2005 A stable discretization of the lattice Boltzmann equation for simulation of incompressible two-phase flows at high density ratios. *J. Comp. Phys.* **206**, 16–47.

Oron, A., Davis, S. H. & Bankoff, G. 1997 Long-scale evolution of thin liquid films. *Rev. Mod. Phys.* **69**, 931–980.

Pismen, L. M. & Pomeau, Y. 2000 Disjoining potntial and spreading of thin liquid layers in the diffuse-interface model coupled to hydrodynamics. *Phys. Rev.* E **62**, 2480–2492.

Podgorski, T., Flesselles, J. M. and Limat, L. 2001 Corners, Cusps and pearls in running drops. *Phys. Rev. Lett.* **87**, 036102.

Quéré, D. 1991 On the minimal velocity of forced spreading in partial wetting. *C. R. Acad. Sci. Paris II* **313**, 313–318.

Rame, E., Garoff, S. & Willson, W. R. 2004 Characterizing the microscopic physics near moving contact lines using dynamic contact angle data. *Phys. Rev.* E **70**, 031608.

Sbragaglia, M., Benzi, R., Biferale, L., Succi, S. Sugiyama, K. & Toschi, F. 2007 Generalized lattice Boltzmann method with multi-range pseudo-potential. *Phys. Rev.* E **75**, 026702.

Sbragaglia, M., Benzi, R., Biferale, L., Succi, S. & Toschi, F. 2006 Surface roughness-hydrophobicity coupling in microchannel and nanochannel Flows. *Phys. Rev. Lett.* **97**, 204503.

Sedev, R. V. & Petrov, J. G. 1991 The critical condition for transition from steady wetting to film entrainment. *Colloids. Surf.* **53**, 147–156.

Seppecher, P. 1996 Moving contact lines in the Cahn–Hilliard theory. *Intl J. Eng. Sci.* **34**, 977–992.

Shan, X. 2006 Analysis and reduction of the spurious current in a class of multiphase lattice Boltzmann models. *Phys. Rev.* E **73**, 047701.

Shan, X. & Chen, H. 1993 Lattice Boltzmann model for simulating flows with multiple phases and components. *Phys. Rev.* E **47**, 1815–1819.

Shan, X. & Chen, H. 1994 Simulation of nonideal gases and liquid–gas phase transitions by the lattice Boltzmann equation. *Phys. Rev.* E **49**, 2941–2948.

https://doi.org/10.1017/S0022112008003649 Published online by Cambridge University Press

Simpkins, P. G. & Kuck, V. J. 2003 On air entrainment in coatings. *J. Colloid Interface Sci.* **263**, 562.

Snoeijer, J. H. 2005 Free-surface flows with large slopes: beyond lubrication theory. *Phys. Fluids* **18**, 021701.

Snoeijer, J. H., Delon, G., Fermigier, M. & Andreotti, B. 2006 Avoided critical behaviour in dynamically forced wetting. *Phys. Rev. Lett.* **96**, 174504.

Snoeijer, J. H., Andreotti, B., Delon, G. & Fermigier, M. 2007 Relaxation of a dewetting contact line: Part 1; a full-scale hydrodynamic calculation. *J. Fluid Mech.* **579**, 63–83.

Somalinga, S. & Bose, A. 2000 Numerical investigation of boundary conditions for moving contact line problems. *Phys. Fluids* **12**, 499.

Succi, S. 2001 *The Lattice Boltzmann Equation*. Oxford Science.

Thompson, P. A. & Robbins, M. O. 1989 Simulation of contact line motion, Slip and the dynamic contact angle. *Phys. Rev. Lett.* **63**, 766.

Voinov, O. V. 1976 Hydrodinamics of wetting. *Fluid Dyn.* **11**, 714.

Wagner, A. J. 2003 The origin of spurious velocities in lattice Boltzmann. *Intl J. Mod. Phys.* B **17**, 193–196.

Wolf-Gladrow, D. 2000 *Lattice–Gas Cellular Automata And Lattice Boltzmann Models*. Springer.

Yuan, P. & Schaefer, L. 2006 Equations of state in a lattice Boltzmann model. *Phys. Fluids* **18**, 042101.

Zhang, J. & Kwok, D. Y. 2006 Contact line and contact angle dynamics in superhydrophobic channels. *Langmuir* **22**, 4998–5004.

https://doi.org/10.1017/S0022112008003649 Published online by Cambridge University Press